Wideband Koch Fractal Technique for Intelligent Reflecting Surface Application

Nur Syahirah Mohd Yaziz[1], Mohamad Kamal A. Rahim[1], Farid Zubir[2†], Salah I. Yahya[3], Noor Asmawati Samsuri[1], and Taufiqqurrachman[1]

[1]Advanced RF and Microwave Research Group, Faculty of Electrical Engineering, Universiti Teknologi Malaysia, Johor Bahru, Johor, Malaysia

[2]Wireless Communication Centre, Faculty of Electrical Engineering, Universiti Teknologi Malaysia, Johor Bahru, Johor, Malaysia

[3]Department of Computer Technology Engineering, College of Technical Engineering, Al-Hadba University, Mosul, Iraq

***Abstract*—This paper presents a wideband X-band intelligent reflecting surface (IRS) based on a novel combined inward–outward Koch fractal metasurface. The proposed unit cell integrates inward and outward Koch fractal geometries to increase the effective electrical current path and support multiple resonant modes, thereby enhancing the reflection bandwidth while maintaining a compact single-layer structure. A 300 × 300 mm² IRS prototype was designed, fabricated, and experimentally validated. Simulation results demonstrate a reflection phase bandwidth of 2.40 GHz (8.95–11.35 GHz), while measurements confirm a bandwidth of 2.25 GHz (8.90–11.15 GHz), corresponding to a fractional bandwidth of 22.44%. The measured reflection magnitude and phase responses are in good agreement with the simulated results. System-level experiments conducted in a non-line-of-sight environment further demonstrate that the proposed IRS improves the received signal strength by more than 15 dB compared with the case without an IRS, confirming its capability to redirect electromagnetic waves and enhance wireless coverage effectively. The combination of wideband performance, compact single-layer construction, and experimentally verified signal enhancement demonstrates the potential of the proposed combined Koch fractal IRS for next-generation intelligent wireless communication systems.**

***Index Terms*—Fractal geometry, Intelligent reflecting surface, Koch fractal, Metasurface, Reflection phase, Wideband metasurface, X-band**

I. Introduction

Intelligent reflecting surfaces (IRSs) have emerged as a promising technology for next-generation wireless communication systems by enabling the creation of programmable electromagnetic environments. An IRS consists of a large array of subwavelength metasurface unit cells whose reflection characteristics can be dynamically controlled to manipulate incident electromagnetic waves. Through independent adjustment of the reflection phase of each unit cell, IRSs enable beam steering, beam focusing, and wavefront shaping, thereby improving wireless coverage, spectral efficiency, and energy efficiency (Huang, et al., 2019).

IRS implementations can generally be classified into two categories (Dharmawansa, Atapattu and Renzo, 2021). The first consists of infrastructure-assisted IRSs integrated into building walls, ceilings, or other fixed structures, where a software controller dynamically adjusts the reflected electromagnetic waves to enhance wireless communication performance (Bao and Guo, 2025; Magbool, et al., 2025). The second category comprises embedded IRSs integrated into smart objects, such as wearable devices and sensor-enabled textiles, which communicate by modulating and backscattering radio-frequency signals transmitted by existing wireless infrastructure (Kobyakov and Zakharian, 2023).

The electromagnetic behavior of an IRS is fundamentally determined by its constituent metasurface unit cells. Depending on the unit-cell design, metasurfaces can manipulate incident electromagnetic waves by controlling their reflection, transmission, or absorption characteristics (Dai, et al., 2021; Gros, et al., 2021; Han, et al., 2024). The phase and amplitude responses of a metasurface are strongly influenced by several design parameters, including the unit-cell geometry, dimensions, rotational symmetry, and substrate material properties (Cheng, et al., 2017; Pei, et al., 2021; Costa and Borgese, 2021; Ke, et al., 2020; Lee and Hong, 2025). Although numerous metasurface designs have demonstrated excellent control over a single electromagnetic degree of freedom, such as phase, amplitude, or polarisation, simultaneously achieving broadband operation while maintaining high reflection efficiency remains a significant design challenge (Alamzadeh, et al., 2021).

ARO-The Scientific Journal of Koya University
Vol. XIV, No.2 (2026), Article ID: ARO.12928. 10 pages
DOI: 10.14500/aro.12928
Received: 08 March 2026; Accepted: 16 August 2026
Regular research paper; Published: 18 September 2026
†Corresponding author's e-mail: faridzubir@utm.my

Among various unit-cell geometries, square-shaped metasurfaces have attracted considerable attention because of their simple fabrication, polarisation-independent response, high angular stability, and favorable reflection characteristics (Yaziz, et al., 2023). However, conventional square geometries generally suffer from limited operational bandwidth, restricting their applicability in broadband wireless systems and IRS applications.

Fractal geometries provide an effective approach for overcoming bandwidth limitations by introducing self-similar structures that increase the effective electrical length without enlarging the physical dimensions of the unit cell. Fractal theory, originally introduced by Benoit Mandelbrot in 1975, has been extensively applied in microwave engineering to realize compact, broadband electromagnetic structures. Among various fractal geometries, the Koch fractal has been widely adopted because it increases the current path length, generates multiple resonant modes, and improves impedance matching, thereby enhancing bandwidth while maintaining a compact footprint. Although inward and outward Koch fractal geometries have individually demonstrated improved electromagnetic performance, their combined implementation within a single metasurface unit cell has received limited attention. Existing studies primarily investigate either inward or outward Koch configurations independently, leaving the potential advantages of integrating both fractal geometries largely unexplored. Besides, the influence of such a hybrid configuration on reflection characteristics, operating bandwidth, surface current distribution, and received power has not been comprehensively investigated.

To address these limitations, this paper proposes a novel combined inward–outward Koch fractal metasurface operating in the X-band frequency range. By integrating inward and outward Koch fractal geometries into a single unit-cell structure, the proposed design increases the effective current path length and supports multiple resonant modes, leading to enhanced reflection efficiency and significantly improved bandwidth compared with conventional square and individual Koch fractal configurations. The proposed metasurface is comprehensively evaluated through both numerical simulation and experimental measurement. Its performance is assessed in terms of reflection magnitude, reflection phase, resonance frequency, bandwidth, surface current distribution, and normalized received power to provide a detailed understanding of the underlying electromagnetic behavior. Section II describes the design methodology and configuration of the proposed combined Koch fractal metasurface. Section III presents the simulated and measured results, together with a comprehensive performance analysis. Section IV presents a comparative study with previously reported metasurfaces. Finally, Section V concludes the paper and summarizes the main findings.

II. Design Concept

To determine whether a wideband response was achievable, this study investigated the connection between inward and outward Koch fractal structures. Rather than relying on the fundamental square structure's characteristically limited bandwidth, the Koch fractal design is expected to provide a broader bandwidth. The Koch fractal structure was selected for the reflecting metasurface because it allows for the extension of the unit cell's side length without altering its overall dimensions. Koch curves, a well-known type of fractal, have been widely employed to simplify design methods while maintaining wideband frequency coverage (Karim, et al., 2010).

The initial configuration consists of a solid square patch with side length a, fabricated on a dielectric substrate characterised by relative permittivity ε_r and thickness h. At this stage, the square exhibits a perimeter of 4a and an area of a^2. Equations (1) and (2), which involve the effective dielectric constant ε_{eff}, ε_r, and the speed of light c, require the electrical length (L) of the patch element to be approximately half the free-space wavelength for the resonance frequency (f_r) to occur (Pozar, 2012). This study presents a metasurface reflector design that combines outward and inward angles based on fractal geometry.

$$f_r = \frac{c}{2L\sqrt{\varepsilon_{eff}}} \tag{1}$$

$$\varepsilon_{eff} = \sqrt{\frac{\varepsilon_r + 1}{2}} \tag{2}$$

The fractal transformation is introduced by subdividing each side of the square into three equal segments. The central segment is replaced by two inclined segments forming an outward and inward equilateral triangular feature. This operation increases the boundary length while preserving the symmetry of the original square. Fig. 1 illustrates the iterative process used to create the curve. In the second segment, the line is rotated by 45° and –45°, and then scaled to one-third and translated in the final segment. The value of the hypotenuse, h, can be calculated using Equation (3). The fractal configuration, incorporating both outward and inward components, is shown in Fig. 2.

$$h = \sqrt{\left(\frac{l_n}{2}\right)^2 + \left(\sin\left(\frac{\pi}{3}\right)\left(\frac{l_n}{3}\right)^2\right)} \tag{3}$$

By reiteratively applying this transformation to all newly generated boundary segments, a combination of inward and outward is formed. After n iterations, the perimeter of the resulting geometry is given by equation (4) (Zhang, et al., 2025). The Koch element is defined as the solid region enclosed by this fractal boundary. While the perimeter increases with iteration order, the enclosed area converges to a finite value, ensuring that the physical area remains bounded. Electromagnetically, the complex boundary promotes extended current paths and enhanced capacitive loading at the fractal corners. As a result, the effective electrical length increases with iteration order, leading to a reduced resonance frequency that can be approximated by equation (5). Therefore, this square is to combine the

Koch inward and outward transformation provides a clear conceptual framework for bandwidth enhancement and resonance control.

$$P_n = 4a\left(\frac{4}{3}\right)^n \quad (4)$$

$$f_r \approx \frac{c}{2P_n\sqrt{\varepsilon_{eff}}} \quad (5)$$

Fig. 3 illustrates the design evolution of the proposed wideband metasurface unit cell based on the Koch fractal geometry. A systematic parametric design approach was adopted to investigate the influence of successive geometric modifications on the electromagnetic response. As shown in Fig. 3, the design process begins with a conventional square metallic patch. Subsequently, an outward Koch fractal is introduced along the patch boundaries to increase the effective electrical length. In the second stage, an inward Koch fractal is incorporated to further modify the current distribution and enhance capacitive coupling. Finally, the inward and outward Koch fractal configurations are combined to form the proposed unit cell, which exhibits significantly improved broadband characteristics.

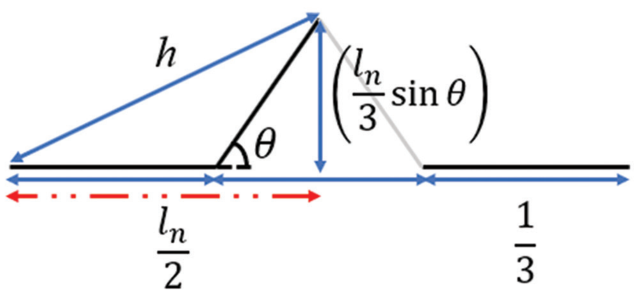

Fig. 1. The primary segments of the Koch fractal (Karim, et al., 2010).

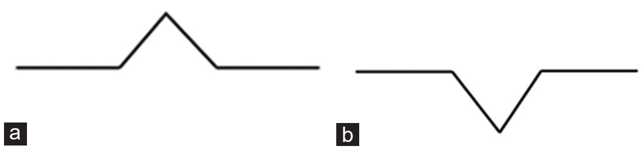

Fig. 2. Illustration of fractal geometry: (a) Outward Koch fractal and (b) inward Koch fractal.

Both Koch fractal configurations employ a 45° iteration angle, producing an interconnected metallic geometry that increases the electrical path length while maintaining a compact physical footprint. The proposed unit cell has dimensions of 11.43 mm × 11.43 mm (W × L) and is fabricated on an F4BMX220 substrate with a thickness of 1.51 mm, relative permittivity (εr) of 2.2, and a loss tangent of 0.0009. The metallic pattern is modeled using copper with an electrical conductivity of $\sigma = 5.8 \times 10^7$ S/m, while a continuous copper ground plane is employed on the opposite side of the substrate to ensure near-unity reflection of the incident electromagnetic waves.

The electromagnetic characteristics of the proposed metasurface are analysed using the CST Microwave Studio frequency-domain solver. Floquet ports are assigned along the propagation (z-) direction, whereas periodic unit-cell boundary conditions are imposed in the x- and y-directions to emulate an infinitely periodic metasurface. Figure 4(a) illustrates the fabricated prototype of the proposed metasurface. Since the primary objective of this work is the proposed combined inward - outward Koch fractal structure shown in (Fig. 4b), only the optimized geometrical parameters of the final unit cell are presented in Table I.

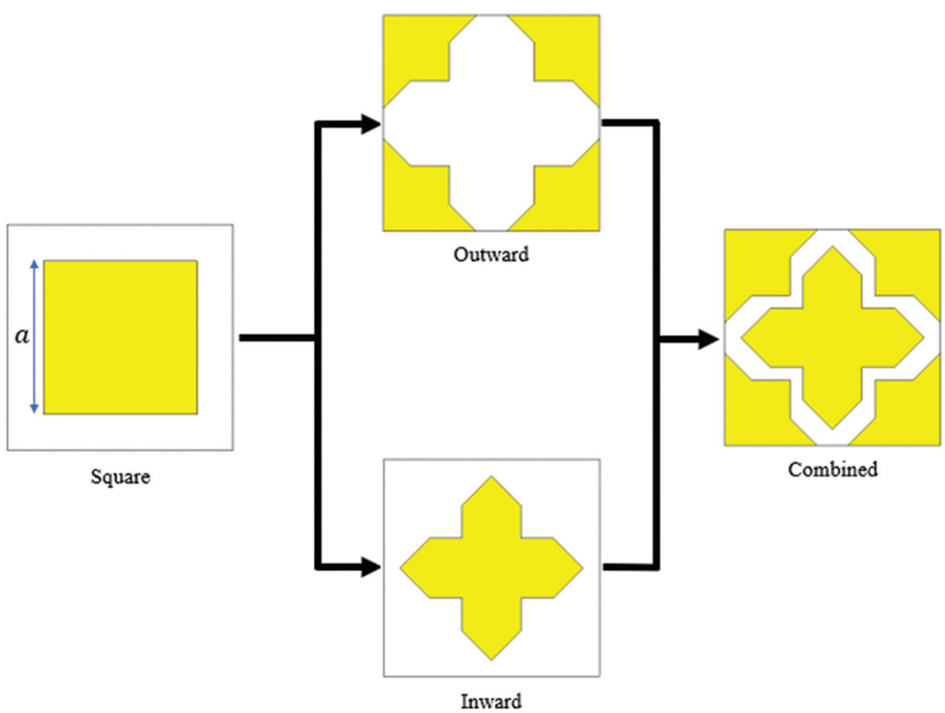

Fig. 3. Configuration of the outward Koch fractal, inward Koch fractal, and the combined fractal structure.

 http://dx.doi.org/10.14500/aro.12928

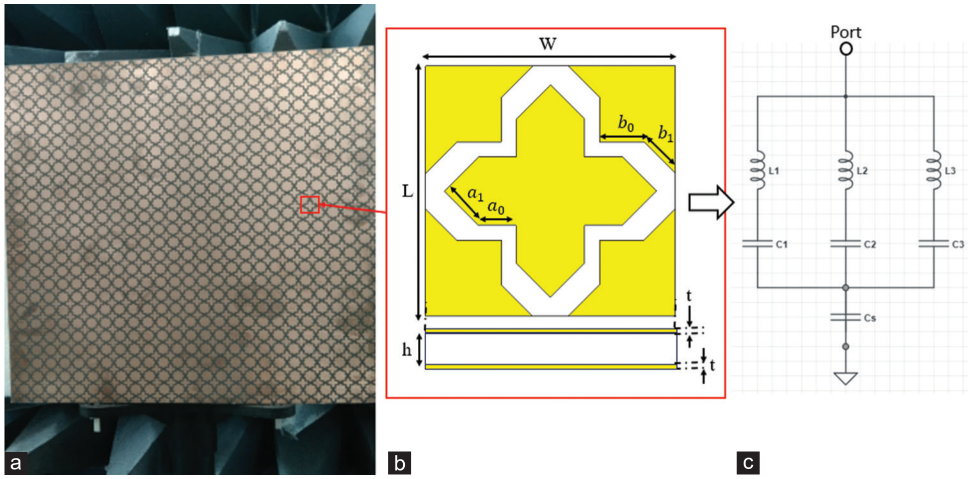

Fig. 4. (a) Metasurface prototype structure, (b) the combined fractal structure design, (c) equivalent circuit.

TABLE I
Unit Cell Dimension of the Combined Fractal Structure

Parameters	Dimension (mm)	Dimension in λ_g at resonance
W	11.430	0.3810
L	11.430	0.3810
a_0	2.340	0.0780
a_1	1.660	0.0553
b_0	2.870	0.0956
b_1	2.030	0.0676
h	1.510	0.0500
t	0.035	0.0012

To provide physical insight into the resonance mechanism, an equivalent lumped-element circuit model is established, as illustrated in (Fig. 4c). The distributed metallic resonator is represented by three parallel LC resonant branches together with an additional substrate capacitance. Each LC branch corresponds to a dominant current path identified from the surface current distribution, thereby establishing a direct relationship between the physical geometry and its equivalent electrical response.

The inductive elements (L_1, L_2, and L_3) represent the magnetic energy stored by surface currents flowing along different sections of the metallic resonator. Specifically, L_1 and L_3 correspond to the current paths along the left and right fractal arms, whereas L_2 represents the current flowing through the upper and lower interconnected sections. The fractal geometry effectively elongates the current paths, thereby increasing the equivalent inductance and reducing the resonant frequency without enlarging the physical dimensions of the unit cell.

The capacitances (C_1, C_2, and C_3) arise from the fringing electric fields generated across the narrow gaps between adjacent metallic edges. C_1 and C_3 represent the edge coupling on the left and right sections of the resonator, while C_2 models the coupling between the upper and lower metallic regions. In addition, the substrate capacitance (C_S) represents the electric-field coupling between the metallic resonator and the continuous ground plane through the dielectric substrate. The magnitude of C_s is primarily determined by the substrate permittivity, substrate thickness, and the effective overlap area between the resonator and the ground plane.

The overall input impedance of the proposed unit cell can be expressed as (Borgese et al, 2020).

$$Z_{eq} = \left(\frac{1}{Z_1} + \frac{1}{Z_2} + \frac{1}{Z_3}\right)^{-1} + \frac{1}{j\omega C_s}, \quad (6)$$

where

$$Z_i = j\omega L_i + \frac{1}{j\omega C_i}, i = 1,2,3 \quad (7)$$

The reflection coefficient under normal incidence is determined by (Pozar, 2012).

$$\Gamma = \frac{Z_{eq} - \eta_0}{Z_{eq} + \eta_0}, \quad (8)$$

where $\eta_0 = 377\Omega$ is the intrinsic impedance of free space.

The proposed equivalent circuit reveals that the unit cell operates through multiple distributed resonant modes rather than a single dominant resonance. Each LC branch resonates at a slightly different frequency due to the distinct electrical lengths and coupling capacitances associated with the corresponding fractal sections. As the operating frequency increases, these resonances progressively overlap, resulting in a broader impedance-matching region. Consequently, the reflection magnitude remains close to unity while the reflection phase varies smoothly over a wider frequency range. This distributed resonance mechanism explains the superior broadband performance of the proposed combined fractal structure metasurface compared with conventional single-resonator unit cells.

III. Results and Discussion

This section presents and discusses the simulation results of the proposed metasurface design. The influence of the Koch fractal configuration on the electromagnetic performance is systematically investigated. For each configuration, the reflection magnitude, reflection phase, surface current distribution, and normalized received power are analysed. Furthermore, the operational bandwidth of each Koch fractal configuration is evaluated and compared.

A. Simulation Results

The simulations were performed using the CST Microwave Studio frequency-domain solver. A 2 × 2 array of unit cells was employed to ensure compatibility with the 22.86 × 22.86 mm^2 aperture of the standard square waveguide, as illustrated in Fig. 5. The arrayed configuration forms a metasurface sample that completely covers the waveguide aperture, thereby enabling accurate electromagnetic characterization under waveguide excitation. Fig. 5 illustrates the four metasurface configurations investigated in this study. (Fig 5a) presents the conventional square patch, (Fig. 5b) shows the outward Koch fractal configuration, (Fig. 5c) depicts the inward Koch fractal configuration, and (Fig. 5d) illustrates the proposed combined fractal structure.

From (Fig. 6a), it is observed that all Koch fractal metasurface configurations exhibit reflection magnitudes greater than −1.5 dB across the operating band, corresponding to reflection efficiencies exceeding 70%. Among the investigated designs, the combined Koch fractal structure achieves the highest reflection performance, with a reflection magnitude of approximately −0.7 dB, corresponding to a reflection efficiency of about 85%. This represents an improvement over the conventional square configuration (70%), the outward Koch fractal (72%), and the inward Koch fractal (77%). The enhanced reflection performance is attributed to the integration of the inward and outward Koch fractal geometries, which increases the effective surface current path length and strengthens electromagnetic coupling. These effects improve the impedance matching between the metasurface and free space, thereby reducing reflection loss and maintaining high reflection efficiency over the operating frequency range.

Furthermore, the reflection phase response shown in (Fig. 6b) is analysed within the phase interval of −90°–+90° to determine the operational bandwidth of the proposed metasurface reflector. The ±90° reflection phase criterion is adopted because it corresponds to the approximately linear region of the phase response, where the unit cell exhibits high reflection efficiency, stable phase sensitivity, and predictable electromagnetic behavior. Beyond this range, the reflection phase varies rapidly near resonance and gradually approaches the asymptotic limits of ±180°, resulting in increased phase non-linearity and degraded beamforming accuracy. Although practical IRS implementations generally require a complete 360° reflection phase coverage, this capability is commonly realized using multiple discrete phase states or electronically reconfigurable unit cells rather than the response of a single passive element. Therefore, evaluating the operational bandwidth within the ±90° phase interval provides a practical and physically meaningful assessment of the usable frequency range for efficient wavefront manipulation (Zhu, Zhao and Feng, 2013).

Table II summarizes the operational bandwidth achieved by the four Koch fractal configurations. The conventional square configuration exhibits the narrowest operating range, extending from 9.15 to 10.55 GHz, corresponding to an absolute bandwidth of 1.40 GHz and a fractional bandwidth of 14.21%. This configuration serves as the reference for evaluating the bandwidth enhancement introduced by the fractal geometries. Introducing the outward Koch fractal broadens the operating frequency range to 8.85–10.70 GHz, resulting in an absolute bandwidth of 1.85 GHz and

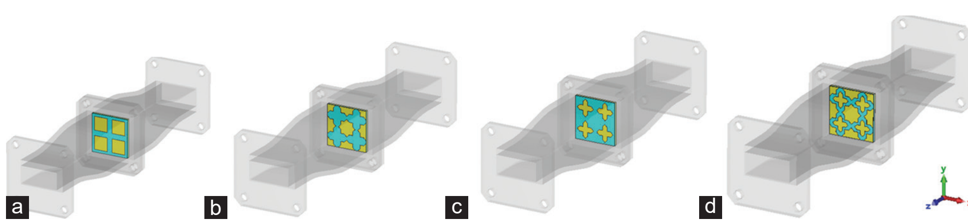

Fig. 5. Simulation 2 × 2-unit cell metasurface reflector using a waveguide port: (a) Conventional square, (b) outward Koch fractal, (c) inward Koch, and (d) combined fractal structure configuration.

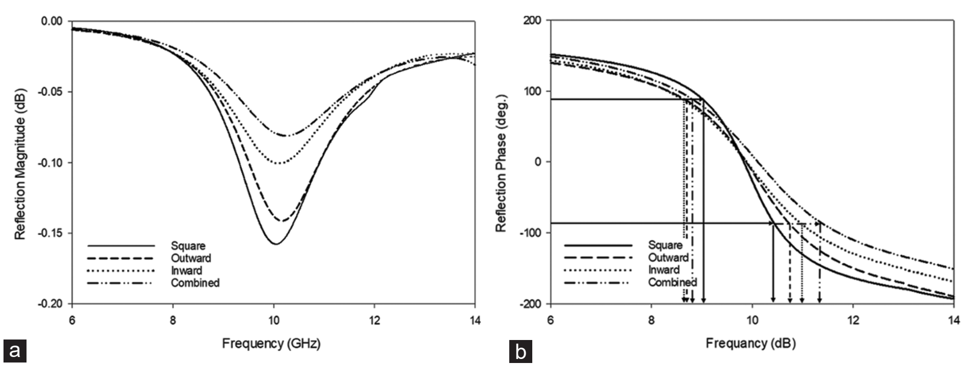

Fig. 6. Simulated reflection (a) magnitude and (b) phase results for different Koch fractal configurations of the unit cell.

http://dx.doi.org/10.14500/aro.12928

a fractional bandwidth of 18.93%. This corresponds to a bandwidth enhancement of 0.45 GHz (32.14%) compared with the square configuration. The improvement is attributed to the additional resonant current paths introduced by the outward fractal edges, which extend the effective operating frequency range. The inward Koch fractal further increases the bandwidth to 2.05 GHz over the frequency range of 8.90–10.95 GHz, achieving a fractional bandwidth of 20.66%. Relative to the square configuration, this represents a bandwidth enhancement of 0.65 GHz (46.43%). The inward fractal perturbations enhance electromagnetic coupling and promote multiple resonant modes, thereby improving the broadband reflection characteristics.

Among all configurations, the combined Koch fractal structure exhibits the best bandwidth performance, operating from 8.95 to 11.35 GHz with an absolute bandwidth of 2.40 GHz and a fractional bandwidth of 23.65%. Compared with the conventional square configuration, it achieves the largest bandwidth enhancement of 1.00 GHz (71.43%). This improvement is attributed to the synergistic interaction of the inward and outward Koch fractal features, which produces more extensive surface current distributions, multiple resonant current paths, and improved impedance matching over a wider frequency range. The broader current distribution observed in Fig. 7 further confirms the excitation of multiple resonances, leading to enhanced broadband performance. Overall, the results demonstrate that increasing the geometric complexity of the Koch fractal progressively broadens the operational bandwidth while maintaining high reflection efficiency. Consequently, the proposed combined fractal structure configuration offers the widest frequency coverage and superior reflection performance among the investigated designs, making it a promising candidate for broadband X-band metasurface reflector applications. The bandwidth enhancement for each configuration is calculated using (9), with the conventional square configuration adopted as the reference following (Dewan, et al., 2013).

$$\%\text{BW improvement} = \frac{\text{New bandwidth} - \text{Initial bandwidth}}{\text{Initial bandwidth}} \times 100\% \quad (9)$$

Fig. 7 illustrates the simulated surface current distributions of the proposed combined fractal metasurface under two orthogonal incident wave polarizations at 9 GHz, 10 GHz, and 11 GHz. Figs. 7a and b correspond to the surface current distributions for the H-field and E-field polarizations, respectively. For the H-field polarisation shown in Fig. 7a, the induced surface current is primarily concentrated along the +x and −x directions of the fractal structure. The high current density observed along these sections indicates that these conductive paths serve as the dominant resonant elements, resulting in strong electromagnetic coupling with the incident wave. Conversely, for the E-field polarisation in Fig. 7b, the surface current is mainly distributed along the +y and −y directions, while a comparatively weaker current is observed along the ±x directions. This complementary current distribution demonstrates that the metasurface effectively supports both orthogonal polarizations by exciting different resonant paths within the fractal geometry.

TABLE II
Simulated Bandwidth Performance of Metasurface Koch Fractal Configuration

Koch fractal configuration	Frequency coverage (GHz)	Bandwidth		Bandwidth improvement	
		GHz	Percentage	GHz	Percentage
Square	9.15–10.55	1.40	14.21	-	-
Outward	8.85–10.70	1.85	18.93	0.45	32.14
Inward	8.90–10.95	2.05	20.66	0.65	46.43
Combined	8.95–11.35	2.40	23.65	1.00	71.43

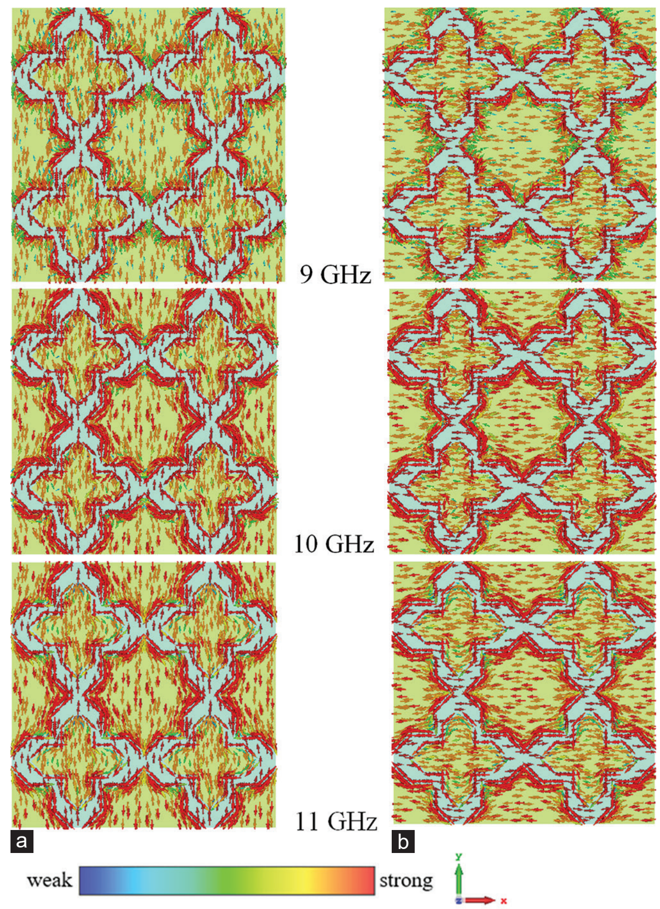

Fig. 7. Surface current of combined fractal structure at (a) H-field and (b) E-field at 9 GHz, 10 GHz and 11 GHz.

Moreover, the overall current distributions remain highly consistent at 9 GHz, 10 GHz, and 11 GHz, with only slight variations in current magnitude. The preservation of the current pattern across the operating band indicates that the same resonant mechanism is maintained over a wide frequency range, thereby ensuring stable electromagnetic behavior. This consistent surface current distribution confirms that the combined fractal geometry effectively confines electromagnetic energy and supports multiple resonant paths, contributing to the enhanced impedance bandwidth and broadband performance observed in the reflection characteristics.

B. Measurement Results

After confirming the wideband performance of the proposed metasurface through full-wave simulations, experimental measurements were conducted to validate its practical performance. A prototype of the combined fractal metasurface reflector (IRS) was fabricated with overall dimensions of 300 × 300 mm^2, consisting of a periodic array of the proposed unit cells. Fig. 8 illustrates the experimental measurement setup used to characterize the fabricated metasurface. The measurements were performed to verify the reflection characteristics and evaluate the agreement between the simulated and measured results.

As shown in Fig. 9a, the simulated reflection magnitude exhibits a single resonance at 10 GHz with a minimum value of −0.09 dB. The measured prototype also resonates at 10 GHz with a reflection magnitude of −0.30 dB, indicating only a slight increase in reflection loss. Fig. 9b compares the simulated and measured reflection phase responses, where both exhibit a 0° reflection phase at 10 GHz, confirming that the fabricated prototype preserves the designed resonance frequency.

The simulated phase bandwidth extends from 8.95 to 11.35 GHz (2.40 GHz), whereas the measured bandwidth ranges from 8.90 to 11.15 GHz (2.25 GHz). The slight reduction in measured bandwidth is attributed to fabrication tolerances, uncertainties in the substrate dielectric properties, conductor and dielectric losses, minor waveguide fixture misalignment, and measurement uncertainties. Nevertheless, the measured reflection magnitude and phase responses closely follow the simulated characteristics over the entire operating frequency range, demonstrating good agreement between simulation and experiment and validating the proposed combined fractal metasurface for wideband reflection.

Table III summarizes the bandwidth comparison between the waveguide simulation and the VNA measurement. The measured prototype achieves a fractional bandwidth of 22.44%, compared with the simulated value of 23.65%, corresponding to a bandwidth difference of only 0.15 GHz (approximately 1.2%). This close agreement verifies the accuracy of the proposed design and confirms that the fabricated prototype successfully reproduces the predicted wideband reflection performance.

The overall performance of the proposed static IRS was experimentally evaluated under a representative wireless communication scenario. Fig. 10 illustrates the experimental setup used to emulate a practical non-line-of-sight (NLoS) propagation environment. A standard X-band WR-90 gain horn antenna with a gain of 15 dB was employed as the transmitting antenna (Tx) and mounted at a height of 1.5 m on the right-hand side of the measurement area. The fabricated metasurface reflector was positioned at a distance of 50λ_0 from the transmitting antenna, where λ_0 denotes the free-space wavelength at the operating frequency. This separation corresponds to the maximum measurement distance permitted by the available laboratory environment while satisfying the far-field condition. An identical horn antenna was used as the receiving antenna (Rx) and positioned on the opposite side of the measurement setup within a coverage shadow region created by an absorber wall that partially obstructed the line-of-sight (LoS) propagation path. Consequently, the direct electromagnetic wave reaching the receiver was significantly attenuated, thereby establishing a representative NLoS wireless propagation scenario. The proposed static IRS was then oriented to redirect the incident electromagnetic wave toward the receiver at a reflection angle of 45°, corresponding to the intended coverage direction.

Fig. 8. Measurement set-up for the combined fractal structure 2 × 2-unit cell with dimensions of 22.86 mm × 22.86 mm.

TABLE III
PERFORMANCE COMPARISON OF THE SIMULATED AND MEASURED COMBINED FRACTAL STRUCTURE UNIT CELL

Method/Validation approach	Frequency coverage (GHz)	Bandwidth	
		GHz	Percentage
Waveguide simulation	8.95–11.35	2.40	23.65
Measured (VNA)	8.90–11.15	2.25	22.44

As illustrated in Fig. 11, the received power was measured under three different conditions to evaluate the reflection performance of the proposed static IRS: (i) without a reflective structure (non-metallic reference), (ii) using a flat aluminum plate as a conventional metallic reflector, and (iii) using the proposed combined fractal structure metasurface. This comparison enables a direct evaluation of the proposed IRS by assessing its reflection performance against both a non-reflective reference and a conventional metallic reflector under identical NLoS propagation conditions.

For the non-metallic reference, the received power remained approximately −33 dBm across the measured frequency range, indicating substantial propagation loss due to the absence of a reflecting surface. When the flat aluminum plate was introduced, the received power increased to approximately −18 dBm over the entire frequency range due to its high electrical conductivity and near-unity reflection efficiency. Similarly, the proposed combined fractal static IRS achieved an average received power of approximately −18 dBm within its operational bandwidth of 8.95–11.35 GHz, demonstrating efficient electromagnetic

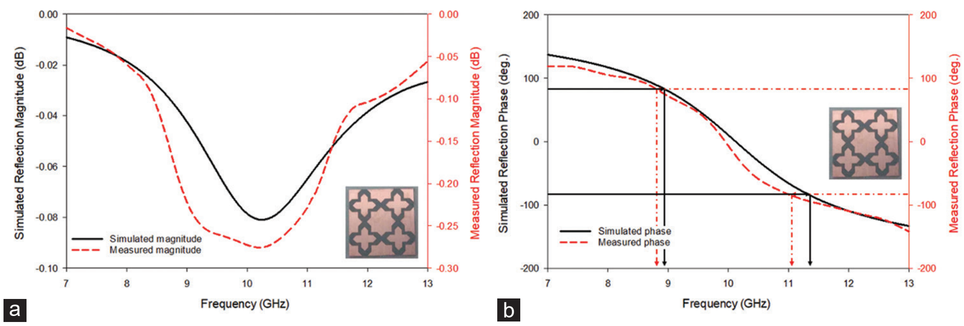

Fig. 9. Simulated and measured reflection (a) magnitude and (b) phase of the combined fractal structure unit cell.

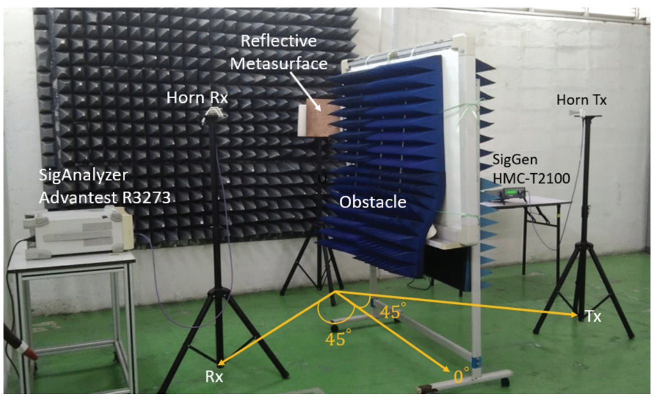

Fig. 10. Measurement setup for evaluating a static intelligent reflecting surface performance under a simulated blockage scenario.

wave reflection throughout the designed X-band operating range. The comparable received power achieved by the proposed static IRS relative to the metallic reflector confirms that the metasurface provides effective passive beam redirection within its operating bandwidth. Unlike conventional metallic reflectors, however, the proposed design offers a compact, lightweight, low-profile structure better suited to practical intelligent wireless communication applications where reduced size, weight, and profile are desirable.

To provide a quantitative comparison, the measured received power was normalized with respect to the aluminum plate, which serves as the reference reflector. Due to its near-ideal reflection characteristics over the operating frequency range, the aluminum plate represents the practical upper bound for passive reflection and therefore provides an appropriate benchmark for evaluating the performance of the proposed static IRS. The normalized received power is defined as in equation (10),

$$P_{norm}\,(dB) = P_{measured} - P_{Al} \tag{10}$$

where $P_{measured}$ is the received power under the test condition, and P_{Al} is the received power measured using the aluminum plate.

As shown in Fig. 12, the proposed static IRS exhibits a normalized received power of approximately 0 dB throughout its operating bandwidth, indicating that it delivers nearly the same received power as the aluminum reference under identical measurement conditions. In contrast, the non-metallic reference produces a normalized received power of approximately −15 dB, confirming a substantial reduction in the reflected signal due to the absence of an effective reflecting surface.

The system-level measurements are consistent with the unit-cell characterization presented in Fig. 9. The measured wideband reflection response, with a fractional bandwidth of 22.44%, enables efficient electromagnetic wave reflection across the operating frequency range, thereby contributing directly to the enhanced received power observed in the static IRS measurements. The close agreement between the waveguide characterization and the prototype measurements demonstrates that the proposed combined fractal metasurface preserves its designed electromagnetic characteristics after fabrication and integration into the full-scale reflector. Overall, the experimental results verify that the proposed static IRS achieves metallic-reflector-like performance within its design bandwidth while simultaneously providing the practical advantages of a planar metasurface, making it a promising candidate for X-band intelligent wireless communication applications.

IV. Comparative Study

Table IV compares the proposed static IRS with recently reported metasurface reflectors in terms of substrate configuration, physical dimensions, operating frequency, and bandwidth. Unlike most existing designs that employ multilayer substrates, the proposed metasurface utilizes a single-layer substrate with a thickness of 1.56 mm, enabling a simpler and more cost-effective fabrication process. Despite its compact configuration, it achieves an operating bandwidth of 8.90–11.15 GHz, which is the widest among the other compared designs. This wideband performance is attributed to the combined fractal structure geometry, which supports multiple resonant modes without requiring additional layers or matching structures. The combination of a single-layer configuration, compact profile, and broad bandwidth demonstrates the competitiveness of the proposed static IRS for practical wideband X-band wireless communication applications.

TABLE IV
Performance Comparison of the Designed Metasurface with the Previously Reported Metasurface in the Literature

References	No. of substrate layers	Total thickness (mm)	Size dimension (mm)	Operating frequency (GHz)	Bandwidth	
					GHz	Percentage
Dai, et al., 2021	2	14.00	592×592	2.10–2.50	0.40	17.40
Gros, et al., 2021	2	-	100×100	26.50–28.00 and 28.50–30.00	1.50 and 1.50	5.50 and 5.50
Pei, et al., 2021	2	2.30	787×206	5.50–6.00	0.50	8.70
Cheng, et al., 2017	2	3.30	173×173	7.10–7.50	0.40	5.50
Ke, et al., 2020	2	7.05	542×410	2.50–2.70	0.20	7.70
Costa and Borgese, 2021	1	1.25	-	9.50–10.50	1.00	10.0
Alamzadeh, et al., 2021	2	3.05	100×8	18.70–19.20	0.50	2.60
This work	1	1.56	300×300	8.90–11.15	2.25	22.44

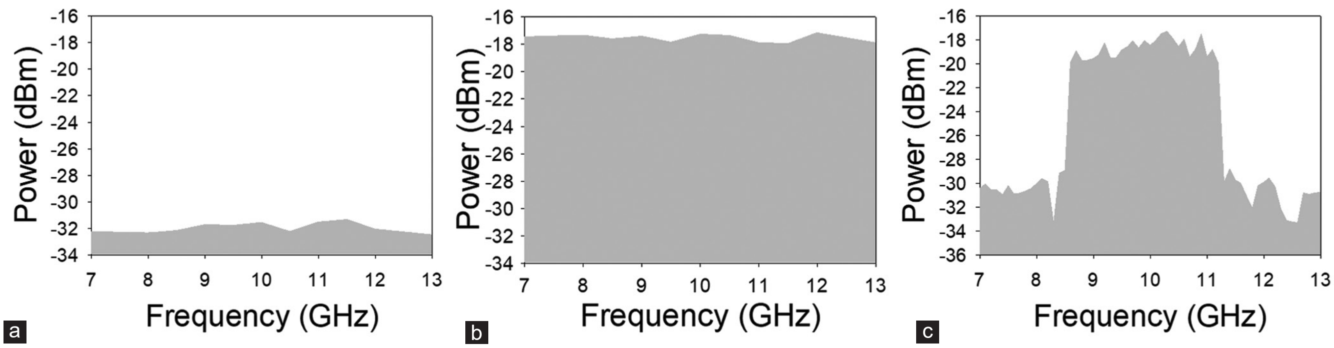

Fig. 11. Received power under experimental test conditions: (a) with a non-metallic structure, (b) with an aluminum plate, and (c) with a static intelligent reflecting surface.

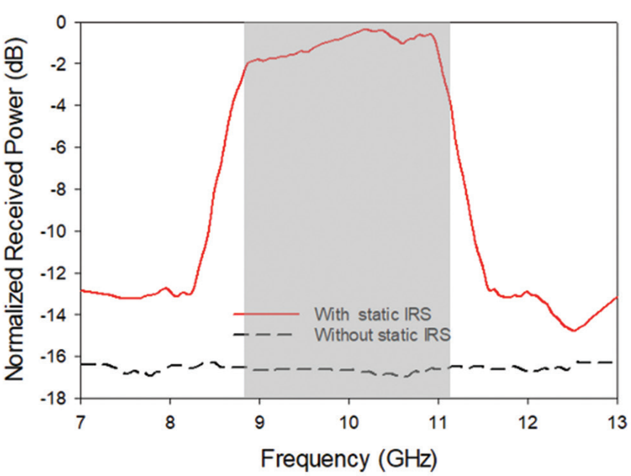

Fig. 12. Measured normalised received power (dB) for the condition with and without static intelligent reflecting surface.

V. Conclusion

This paper presented the design, fabrication, and experimental validation of a wideband static IRS based on a novel combined inward–outward Koch fractal metasurface for X-band applications. The proposed single-layer, low-profile reflector achieved a measured operating bandwidth of 8.90–11.15 GHz (22.44% fractional bandwidth), demonstrating good agreement with the simulated response. The combined fractal geometry effectively generated multiple resonant modes, resulting in stable, wideband reflection characteristics. Experimental system-level measurements further verified the effectiveness of the proposed static IRS under NLoS conditions. Compared with the non-metallic reference, the fabricated prototype improved the received signal strength by more than 15 dB while achieving reflection performance comparable to that of a conventional aluminum reflector within the operating band. These results confirm that the proposed combined fractal metasurface provides an effective wideband, compact, and low-profile IRS solution with strong potential for future intelligent wireless communication systems.

Acknowledgment

This work was supported in part by the Ministry of Higher Education under Fundamental Research under Grant No. 04M34, 5F591 (FRGS/1/2023/TK07/UTM/02/15); in part by the Higher Institution Centre of Excellence, Ministry of Higher Education Malaysia through the Wireless Communication Centre, Universiti Teknologi Malaysia (UTM), under Grant R.J130000.7823.4J610; and in part by the UTM Fundamental Research under Grant Q.J130000.3823.23H92.

References

Alamzadeh, I., Alexandropoulos, G.C., Shlezinger, N., and Imani, M.F., 2021. A reconfigurable intelligent surface with integrated sensing capability. *Scientific Reports*, 11(1), p.21837.

Bao, D., and Guo, R., 2025. A dual function intelligent reflecting surface in integrated radar communication system. *IEEE Transactions on Intelligent Transportation Systems*, 26(3), pp.3471-3481.

Borgese, M., and Costa, F., 2020. A simple equivalent circuit approach for anisotropic frequency-selective surfaces and metasurfaces. *IEEE Transactions on Antennas and Propagation*, 68(12), pp.8098-8107.

Cheng, Z., Sun, B., Pan, W., Cui, J., Wu, X., and Luo, X., 2017. Dynamical beam manipulation based on 2-bit digitally-controlled coding metasurface. *Scientific Reports*, 7, p.42302.

Costa, F., and Borgese, M., 2021. Electromagnetic model of reflective intelligent surfaces. *IEEE Open Journal of the Communications Society*, 2, pp.1577-1589.

Dai, Y., Guan, Y.L., Leung, K.K., and Zhang, Y., 2021. Reconfigurable intelligent surface for low-latency edge computing in 6G. *IEEE Wireless Communications*, 28(6), pp.72-79.

Dewan, R., Rahim, S.K.A., Ausordin, S.F., and Purnamirza, T., 2013. The improvement of array antenna performance with the implementation of an artificial magnetic conductor (AMC) ground plane and in-phase superstrate. *Progress in Electromagnetics Research*, 140, pp.147-167.

Dharmawansa, P., Atapattu, S., and Di Renzo, M., 2021. Performance analysis of a two-tile reconfigurable intelligent surface assisted 2 × 2 MIMO system. *IEEE Wireless Communications Letters*, 10(3), pp.493-497.

Gros, J.B., Popov, V., Odit, M.A., Lenets, V., and Lerosey, G., 2021. A reconfigurable intelligent surface at mmWave based on a binary phase tunable metasurface. *IEEE Open Journal of the Communications Society*, 2, pp.1055-1064.

Han, D., Wang, P., Ni, W., Wang, W., Zheng, A., Niyato, D., and Al-Dhahir, N., 2024. Multi-functional RIS integrated sensing and communications for 6G networks. *IEEE Transactions on Wireless Communications*, 23(11), pp.17079-17094.

Huang, C., Zappone, A., Alexandropoulos, G.C., Debbah, M., and Yuen, C., 2019. Reconfigurable intelligent surfaces for energy efficiency in wireless communication. *IEEE Transactions on Wireless Communications*, 18(8), pp.4157-4170.

Karim, M.N.A., Rahim, M.K.A., Majid, H.A., Ayop, O.B., Abu, M., and Zubir, F., 2010. Log periodic fractal Koch antenna for UHF band applications. *Progress in Electromagnetics Research*, 100, pp.201-218.

Ke, J.C., Dai, J.Y., Chen, M.Z., Wang, L., Zhang, C., Tang, W., Yang, J., Liu, W., Li, X., Lu, Y., Cheng, Q., Jin, S., and Cui, T.J., 2021. Linear and nonlinear polarization syntheses and their programmable controls based on anisotropic time-domain digital coding metasurface. *Small Structures*, 2(1), p.2000060.

Kobyakov, A., and Zakharian, A.R., 2023. Estimate of throughput improvement due to a metasurface reflector in 5G millimeter-wave links. *IEEE Antennas and Wireless Propagation Letters*, 22(3), pp.636-640.

Lee, J., and Hong, S., 2025. Piecewise beam training and channel estimation for RIS-aided near-field communications. *IEEE Transactions on Wireless Communications*, 24(1), pp.753-767.

Magbool, A., Kumar, V., Bazzi, A., Flanagan, M.F., and Chafii, M., 2025. Multi-functional RIS for a multi-functional system: Integrating sensing, communication, and wireless power transfer. *IEEE Network*, 39(1), pp.71-79.

Mandelbrot, B.B., 1982. *The Fractal Geometry of Nature*. W.H. Freeman and Company, San Francisco, CA.

Pei, X., Yin, H., Tan, L., Cao, L., Li, Z., Wang, K., Zhang, K., and Björnson, E., 2021. RIS-aided wireless communications: Prototyping, adaptive beamforming, and indoor/Outdoor field trials. *IEEE Transactions on Communications*, 69(12), pp.8627-8640.

Pozar, D.M., 2012. *Microwave Engineering*. 4th ed. John Wiley and Sons, Hoboken, NJ.

Yaziz, N.S.M., Rahim, M.K.A., Zubir, F., and Samsuri, N.A., 2023. A comparison of the bandwidth coverage for different metasurface reflector shapes. In: *Proceedings of the 2023 IEEE International Symposium on Antennas and Propagation and USNC-URSI Radio Science Meeting (AP-S/URSI)*. IEEE, Portland, OR, USA, pp.1423-1424.

Zhang, X., Han, D., Ke, M., Luo, L., Huang, Z., and Zhang, G. 2026. PD Koch complementary fractal UHF antenna based on AMC metasurface. *Sensors (Basel)*, 23, p.1398.

Zhu, B.O., Zhao, J., and Feng, Y., 2013. Active impedance metasurface with full 360° reflection phase tuning. *Scientific Reports*, 3, p.3059.